Lead-212/Bismuth-212 In Vivo Generator Based on Ultrasmall Silver Telluride Nanoparticles

Wang, Runze; Wolterbeek, Hubert Th.; Denkova, Antonia G.

DOI
10.1002/jlcr.4121

Publication date
2024

Document Version
Final published version

Published in
Journal of Labelled Compounds and Radiopharmaceuticals

Journal of Labelled Compounds and Radiopharmaceuticals

WILEY

Journal of Labelled Compounds and Radiopharmaceuticals

RESEARCH ARTICLE OPEN ACCESS

Lead-212/Bismuth-212 In Vivo Generator Based on Ultrasmall Silver Telluride Nanoparticles

Runze Wang | Hubert Th. Wolterbeek | Antonia G. Denkova

Applied Radiation and Isotopes, Department of Radiation Science and Technology, Faculty of Applied Sciences, Delft University of Technology, Delft, The Netherlands

Correspondence: Antonia G. Denkova (a.g.denkova@tudelft.nl)

Received: 31 May 2024 | **Revised:** 24 July 2024 | **Accepted:** 4 August 2024

Funding: The authors received no specific funding for this work.

Keywords: Auger electrons | indium-111 | internal conversion | lead-212/bismuth-212 in vivo generator | radionuclide therapy | silver telluride nanoparticle

ABSTRACT

Radionuclide therapy employing alpha emitters holds great potential for personalized cancer treatment. However, certain challenges remain when designing alpha radiopharmaceuticals, including the lack of stability of used radioconjugates due to nuclear decay events. In this work, ultrasmall silver telluride nanoparticles with a core diameter of 2.1 nm were prepared and radiolabeled with lead-212 using a chelator-free method with a radiolabeling efficiency of 75%. The results from the in vitro radiochemical stability assay indicated a very high retention of bismuth-212 despite the internal conversion effects originating from the decay of ^{212}Pb. To further evaluate the potential of the nanoparticles, they were radiolabeled with indium-111, and their cell uptake and subcellular distribution were determined in 2D U87 cells, showing accumulation in the nucleus. Although not intentional, it was observed that the indium-111-radiolabeled nanoparticles induced efficient tumor cell killing, which was attributed to the Auger electrons emitted by indium-111. Combining the results obtained in this work with other favorable properties such as fast renal clearance and the possibility to attach targeting vectors on the surface of the nanoparticles, all well-known from the literature, these ultra-small silver telluride nanoparticles provide exciting opportunities for the design of theragnostic radiopharmaceuticals.

1 | Introduction

Radionuclide therapy (RNT) is a cancer treatment modality that typically uses radionuclides coupled to targeting vectors to attack metastasized tumors [1]. The effectiveness of RNT has been proven by numerous preclinical and clinical studies of radiopharmaceuticals using alpha (α) and beta minus particles (β^-) [2]. Due to the high linear energy transfer (LET), α particles can directly interact with the DNA molecules of tumor cells, leading to lethal damage such as induction of double-strand breaks (DSBs) [3]. Moreover, DNA damage by α particles is not dependent on the oxygen level or the cell cycle of tumor cells, providing the possibility to destruct tumors having high radiation resistance [4]. Finally, α particles typically have short ranges in tissues (i.e., equal to several cell diameters), making α radiopharmaceuticals very suitable to treat metastatic tumors, while sparing surrounding healthy tissues [5].

Currently in alpha RNT, the application of lead-212/bismuth-212 (^{212}Pb/^{212}Bi, $t_{1/2}$ = 10.6 h and 60.5 min, respectively) in vivo generator is rapidly increasing [6]. Preclinical and clinical evaluation of ^{212}Pb-based radiopharmaceuticals has been extensively reported in the literature for the treatment of breast cancer [7–13], melanoma [14, 15], pancreatic cancer [16, 17], neuroendocrine cancer [18–20], ovarian cancer [21–23], and brain metastases [24]. Moreover, the combination of ^{203}Pb ($t_{1/2}$ = 51.9 h, E_γ = 279.2 keV, 80.94%) and ^{212}Pb has been explored for tumor theragnostic applications [6, 25, 26]. Despite the positive results from these studies, it has been reported that 37% of the daughter nuclide ^{212}Bi is released from

the used chelator complex (e.g., DOTA) due to the internal conversion effect occurring during the decay of ^{212}Pb [27]. Considering the complex in vivo environment, the free $^{212}Bi^{3+}$ ions are not likely to be recaptured by the chelator molecules but will possibly distribute in the body according to their affinity to certain organs (i.e., mostly kidney uptake), leading to undesired radiation burden [28].

Our group has previously shown that the loss of internally converted daughter nuclides can be avoided by incorporating the mother nuclide in core-shell structured gold nanoparticles [29]. In the present work, we studied ultrasmall silver telluride nanoparticles (Ag_2TeNPs) with a core diameter of 2.1 nm and a hydrodynamic diameter of 2.5 nm as a carrier of ^{212}Pb. Besides offering the possibility to retain ^{212}Bi, the small size of these Ag_2TeNPs might also enable renal clearance and penetration into the cell nucleus, providing more reasons to explore such nanoparticles in alpha RNT.

2 | Methods and Materials

2.1 | Materials

Silver nitrate (≥ 99.9%), L-glutathione (≥ 98%), 5/6-carboxyfluorescein succinimidyl ester (FITC-NHS, > 90%) and sodium carbonate (≥ 98%) were ordered from Thermo Fisher Scientific (Landsmeer, the Netherlands). Lead nitrate (≥ 99%), sodium tellurite (99%), and hydrazine hydrate (50% ~ 60%) were purchased from Merck Sigma (Zwijndrecht, the Netherlands). S-2-(4-Isothiocyanatobenzyl)-diethylenetriamine pentaacetic acid (p-SCN-Bn-DTPA, > 90%) and indium-111 ($^{111}InCl_3$ in 0.01 M HCl) were kindly provided by Erasmus Medical Center (Rotterdam, the Netherlands). The ^{224}Ra/^{212}Pb generator was purchased from Oak Ridge National Laboratory (ORNL, Oak Ridge, TN, USA). All chemicals were used as received without further purification. Milli-Q water was obtained from an in-house Milli-Q system (Millipore) and used throughout this study.

2.2 | Elution of the ^{224}Ra/^{212}Pb Generator

^{212}Pb was obtained by slowly eluting the ^{224}Ra/^{212}Pb generator with 500 μL of 2 M HCl, followed by 250 μL of water. The collected ^{212}Pb solution was evaporated on a hot plate until soft dryness. The residual was then redissolved in 500 μL of 0.5 M sodium acetate (NaOAc) buffer (pH 6.0). The elution efficiency of ^{212}Pb ranged from 87% to 99% ($n > 5$).

2.3 | Synthesis of Ultrasmall GSH-Ag_2TeNPs

The synthesis of GSH-Ag_2TeNPs was adapted from a previously reported protocol with minor adjustments [30]. In a typical synthesis, 1.5 mL of 30 mM silver nitrate ($AgNO_3$), 1.5 mL of 15 mM sodium tellurite (Na_2TeO_3), and 1.5 mL of 90 mM reduced L-glutathione (L-GSH) were mixed in an ice bath (0°C). A total of 0.5 mL of hydrazine hydrate (50%–60%, N_2H_4) was then quickly injected into the mixture. The mixture was vigorously mixed for 5 min. The as-prepared GSH-Ag_2TeNPs were washed twice with water (10 mL per wash) and twice with 1 × PBS buffer (pH 7.4, 10 mL per wash) using Amicon centrifuge filters (MWCO = 10 kDa) at 4200 rpm for 20 min at 4°C. The final volume of the GSH-Ag_2TeNPs was adjusted to 2 mL by 1 × PBS and stored at 4°C until further usage. The molar concentration of the GSH-Ag_2TeNPs in this stock solution was around 120 μM ($n > 3$). Detailed calculations can be found in the Supporting Information.

2.4 | Characterizations

The shape and size of the nanoparticles were studied with a JEM-1400 Plus transmission electron microscope (TEM, JEOL) at the acceleration voltage of 120 kV. The UV-vis absorption spectrum of GSH-Ag_2TeNPs was measured using a UV-vis-NIR spectrophotometer (UV-6300PC, VWR). The hydrodynamic diameter and zeta-potential of the nanoparticles were determined using a zeta-sizer (nano-ZS, Malvern). The Ag content in the purified GSH-Ag_2TeNPs was determined using an ICP-MS (NexION® 2000, PerkinElmer) after being dissolved in concentrated nitric acid. The results of the ICP-MS measurements were used to calculate the concentrations of the nanoparticles.

2.5 | Conjugation of FITC on GSH-Ag_2TeNPs

FITC was linked to GSH-Ag_2TeNPs via the NHS-amine reaction. In a typical reaction, 15 μL of 7 mg/mL FITC-NHS in anhydrous DMSO was added to 1 mL of purified GSH-Ag_2TeNPs (20 μM) in 1 × PBS and left to react overnight at room temperature. The produced FITC-Ag_2TeNPs were washed thrice by 1 × PBS (10 mL per wash) using Amicon centrifuge filters (MWCO = 10 kDa) at 4°C and redispersed in 1 mL 1 × PBS. The samples were stored at 4°C and protected from light. To prove the successful linkage of FITC on the nanoparticles, the luminescent spectra of the FITC-Ag_2TeNPs and GSH-Ag_2TeNPs were recorded using a Cary Eclipse fluorescence spectrophotometer (Agilent, $\lambda_{ex} = 495$ nm, $\lambda_{em} = 519$ nm).

2.6 | DTPA Conjugation on GSH-Ag_2TeNPs

One hundred fifty microliters of purified GSH-Ag_2TeNPs was diluted to a total volume of 1 mL by PBS (30 μM). The pH of the solution was adjusted to ~9.0 by adding 0.1 M Na_2CO_3 (typically 38 μL). Fifteen microliters of 13 mg/mL p-SCN-Bn-DTPA (10 × molar excess to GSH-Ag_2TeNPs) in anhydrous DMSO was then added. The reaction was continued at 37°C for 2 h under constant shaking (800 rpm). Unconjugated DTPA was removed by washing the sample thrice (10 mL of 1 × PBS per wash) using Amicon centrifuge filters (MWCO = 10 kDa). The final volume of the DTPA-Ag_2TeNPs dispersion was adjusted to 1.5 mL by 0.2 M HEPES buffer (pH 7.0), passed through a 20 nm syringe filter (GE Healthcare), and stored at 4°C until further use.

2.7 | Colloidal Stability Assay

The GSH-Ag_2TeNPs were dispersed in PBS or 10% fetal bovine serum (FBS) in PBS and incubated at 37°C for 72 h. The UV-vis

spectrum of each sample was recorded every 24 h. In addition, the hydrodynamic diameter of the samples dispersed in PBS was also measured every 24 h using a zeta-sizer.

2.8 | ^{212}Pb-Radiolabeling of GSH-Ag_2TeNPs

In a typical reaction, 1.5 mL of 30 mM silver nitrate ($AgNO_3$), 1.5 mL of 15 mM sodium tellurite (Na_2TeO_3), and 1.5 mL of 90 mM L-glutathione (L-GSH) as well as 37 kBq ^{212}Pb in 20 μL of 0.5 M NaOAc buffer were mixed in an ice bath (0°C). A total of 0.5 mL of hydrazine hydrate (50%–60%, N_2H_4) was quickly injected into the mixture and vigorously stirred for 5 min, followed by the addition of 50 μL of 10 mM EDTA, and further incubated for 10 min. The produced [^{212}Pb]Pb-GSH-Ag_2TeNPs were then washed thrice by water (10 mL per wash) using centrifuge filters (MWCO = 10 kDa) at 4250 rpm for 20 min at 4°C and redispersed in 1 mM EDTA. The radiolabeling efficiency was determined by iTLC (iTLC-SG, Agilent) before washing the nanoparticles using centrifuge filters (EtOH: 10 wt% NH_4OAc = 1:1, n = 3).

2.9 | ^{111}In-Radiolabeling of DTPA-GSH-Ag_2TeNPs

Typically, 166 μL of DTPA-Ag_2TeNPs (13.7 μM) was mixed with 37 MBq of $^{111}InCl_3$. The total volume of this mixture was filled up to 500 μL with 0.2 M HEPES buffer (pH = 7.0) and then reacted at 37°C for 1 h. The obtained [^{111}In]In-DTPA-Ag_2TeNPs were then passed through a PD-10 column using PBS as eluent. The elution was portioned per 500 μL, and the ^{111}In activity in each fraction was determined using an automatic gamma counter (Wallac Wizard^2 2480, Perkin Elmer) to calculate the radiolabeling efficiency.

2.10 | Radiochemical Stability (RCS) Assay

The RCS of [^{212}Pb]Pb-GSH-Ag_2TeNPs after being incubated in 1 mM EDTA for 4 h or 24 h was determined by iTLC using the same mobile phase as described in the previous section (n = 3).

For the ^{111}In-radiolabeled nanoparticles, the fractions containing [^{111}In]In-DTPA-Ag_2TeNPs were combined, and 10 μL of 200 mM DTPA (pH = 7.0) was added to achieve a final DTPA concentration of 1 mM. The mixture was then incubated at 37°C for 24 h before being passed through a PD-10 column to separate the [^{111}In]In-DTPA-Ag_2TeNPs from the free [^{111}In]In-DTPA. The RCS was then calculated by comparing the activity retained in the nanoparticles with the initial activity used to radiolabel the nanoparticles (n = 3).

2.11 | Cell Culture

U87 human glioblastoma cells (ATCC) were cultured in complete Dulbecco's modified Eagle's medium (DMEM) supplemented with 10% FBS and 1% penicillin/streptomycin. The cells were incubated in a humidified environment at 37°C with 5% CO_2.

2.12 | Biocompatibility Studies of GSH-Ag_2TeNPs, ^{nat}Pb-GSH-Ag_2TeNPs, and DTPA-Ag_2TeNPs

U87 cells were seeded on 96-well plates with a cell density of 5000 cells/well. After being preincubated at 37°C for 24 h, the cells were incubated with nonradioactive GSH-Ag_2TeNPs, ^{nat}Pb-GSH-Ag_2TeNPs, and DTPA-Ag_2TeNPs with concentrations ranging from 1 nM to 1000 nM for another 24 h. The viability of the treated cells was determined by CCK-8 assay after washing the cells thrice with PBS. The viability of untreated cells was also measured as a control (n = 3).

2.13 | In Vitro 2D Cell Uptake of [^{111}In]In-DTPA-Ag_2TeNPs

U87 cells were seeded on 12-well plates and preincubated for 24 h (8×10^4 cells/well). On the next day, 1 mL fresh culture medium containing 10, 50, and 100 nM [^{111}In]In-DTPA-Ag_2TeNPs (18 kBq, corresponding to a nanoparticle concentration of 1.5 nM) was added to the cells and incubated for 4 h or 24 h at 37°C. Nonradiolabeled DTPA-Ag_2TeNPs were mixed with the [^{111}In]In-DTPA-Ag_2TeNPs to achieve the chosen nanoparticle concentrations. The cells were then washed three times with PBS and detached by trypsin. The separation of the subcellular fractions was achieved using the Subcellular Protein Fractionation Kit (Thermo Scientific) following the instructions from the manufacturer. The activity of ^{111}In in each cell fraction was measured by an automated gamma counter (Wallac Wizard^2 2480, Perkin Elmer) and summed up to calculate the total uptake. The cell uptake and subcellular distribution of [^{111}In]In-DTPA (18 kBq) were also measured for comparison (n = 3).

2.14 | Confocal Microscope

Approximately 2×10^4 U87 cells/well were seeded on a μ-Slide 8 well high-chambered coverslip (ibidi GmbH, Germany) and preincubated for 24 h. On the next day, the cells were treated with 300 μL of 100 nM FITC-Ag_2TeNPs in culture medium and incubated for another 24 h. The cells were then washed thrice by PBS before being fixed with 4% paraformaldehyde for 10 min and stained with 4′,6-diamidino-2-phenylindole (DAPI, Invitrogen) for 10 min. The confocal images were acquired using a Zeiss LSM 980 confocal microscope and analyzed by Zeiss Zen 3.8 software.

2.15 | In Vitro Cytotoxicity of [^{111}In]In-DTPA-Ag_2TeNPs

The in vitro tumor cell killing efficiency of [^{111}In]In-DTPA-Ag_2TeNPs was determined by performing a colony formation assay. U87 cells were seeded on 12-well plates (8×10^4 cells/well) and preincubated at 37°C for 24 h. [^{111}In]In-DTPA-Ag_2TeNPs with 1, 2, and 3 MBq ^{111}In or 3 MBq [^{111}In]In-DTPA were then added to the cells and incubated at 37°C for 24 h. After the treatment, the cells were washed thrice by PBS, tripsinated, and then reseeded on 6-well plates with a cell density of 500 cells/well and left undisturbed for 14 days to allow colony formation. The culture medium was refreshed every 3

days. On the last day of incubation, the colonies were fixed by 4% (w/v) paraformaldehyde, stained by 1% crystal violet, and counted manually ($n = 3$).

2.16 | Statistical Analysis

Data are expressed as mean ± standard deviation based on at least three independent replicates. Student's *t*-test was used for the comparison between the two samples. For the comparison among multiple samples, one-way or two-way ANOVA test was performed. *p* values: ns $p > 0.05$, $^{*}p \leq 0.05$, $^{**}p \leq 0.01$, $^{***}p \leq 0.001$, and $^{****}p \leq 0.0001$.

3 | Results and Discussion

Nanoparticles with different compositions, sizes, and surface modifications have been extensively studied for medical applications such as drug delivery [31]. However, the mononuclear phagocyte system (MPS) capture of intravenously administrated nanoparticles with a hydrodynamic diameter larger than 5.5 nm usually leads to high liver and spleen uptake. The slow clearance of the nanoparticles from the liver and spleen might lead to potential long-term toxicity to the body which can be caused by the nanoparticles themselves but also by the radionuclides used in case of applying therapeutic radionuclides [32]. One possible way to avoid high MPS capture is to reduce the hydrodynamic diameter of the nanoparticles to less than 5.5 nm, that is, below the threshold value of renal clearance. Renal clearance of nanoparticles through the urinary system is much more efficient than the slow clearance from MPS organs (e.g., liver and spleen), thereby avoiding undesired side effects [33]. In this work, ultrasmall glutathione coated silver telluride nanoparticles (GSH-Ag_2TeNPs) were chosen as carriers of ^{212}Pb because of their favorable pharmacokinetics, their small core size (3 nm), and strong CT contrast provided that sufficient accumulation in tumor tissue is achieved [30]. Radiopharmaceuticals developed based on the GSH-Ag_2TeNPs can provide several benefits including low uptake in healthy tissues as well as imaging by CT/PET or CT/SPECT if radiolabeled with the appropriate radionuclides. Furthermore, sub-5 nm-sized nanoparticles have been reported to passively accumulate in the cell nucleus after internalization [34, 35].

3.1 | Synthesis of GSH-Ag_2TeNPs

The GSH-Ag_2TeNPs were formed by reducing silver salts with hydrazine at 0°C in the presence of L-GSH as capping ligands. The shape and size of the GSH-Ag_2TeNPs were characterized by TEM (Figure 1a) and were found to be quasispherically shaped with a core diameter of 2.1 ± 0.3 nm. Due to the GSH coating on the nanoparticle surface, the number-based hydrodynamic diameter of GSH-Ag_2TeNPs was found to be 2.5 ± 0.1 nm by dynamic light scattering (DLS), slightly larger than the core size (Figure 1b). The high sensitivity of the UV-vis spectrum to size variations of the GSH-Ag_2TeNPs allows for determining the presence of large particles. As shown in Figure 1c, no obvious peaks were observed in the spectrum, further confirming the small size of the GSH-Ag_2TeNPs [30]. The zeta-potential of the GSH-Ag_2TeNPs was found to be −31.4 ± 0.3 mV, suggesting high colloidal stability due to repulsion [36].

3.2 | Colloidal Stability of GSH-Ag_2TeNPs

To confirm the high colloidal stability, the GSH-Ag_2TeNPs were dispersed in PBS or 10% FBS and incubated at 37°C for 72 h. The UV-vis spectrum was recorded every 24 h as an indication of possible size increase or aggregation. As shown in Figure 2, no significant change was observed in the UV-vis spectrum of the samples in either PBS or 10% FBS, indicating high colloidal stability of the GSH-Ag_2TeNPs in these solvents. The high resistance to protein adsorption could be attributed to the zwitterionic coating provided by GSH, which hinders protein binding [37]. The high colloidal stability of the GSH-Ag_2TeNPs in PBS was also demonstrated by monitoring the change of hydrodynamic diameter over 72 h (Figure S1).

3.3 | Preparation of [^{212}Pb]Pb-GSH-Ag_2TeNPs

According to our previous work, it seems that the dissociation of internally converted daughter nuclides can be avoided if incorporating the mother nuclides inside a solid composed of high Z elements such as gold [29, 38, 39]. Therefore, high ^{212}Bi retention might be achieved by incorporating ^{212}Pb in GSH-Ag_2TeNPs (Figure 3).

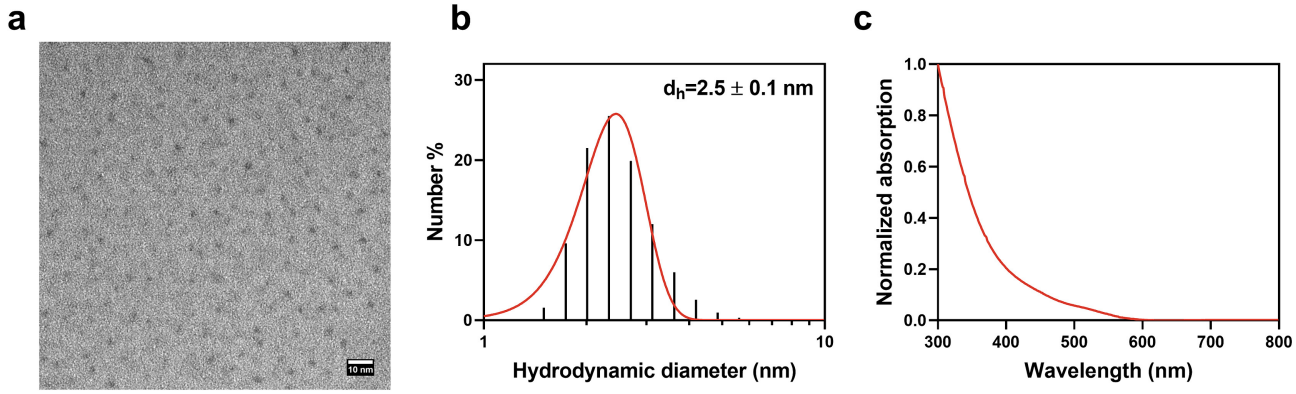

FIGURE 1 | Characterization of GSH-Ag_2TeNPs: (a) TEM image, scale bar = 10 nm; (b) number-based hydrodynamic diameter; (c) normalized UV-vis spectrum. The nanoparticles were dispersed in PBS for the DLS and UV-vis measurements.

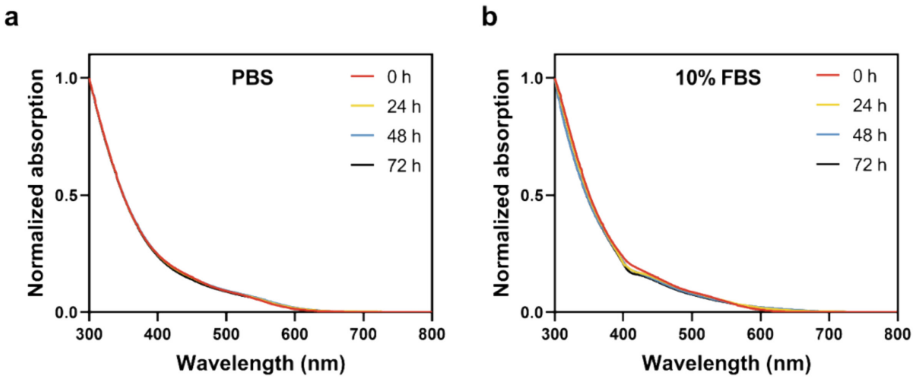

FIGURE 2 | Colloidal stability of GSH-Ag_2TeNPs. The nanoparticles were dispersed in either PBS or 10% FBS in PBS and incubated at 37°C for 72 h. The UV-vis spectrum of GSH-Ag_2TeNPs in (a) PBS and (b) 10% FBS was recorded every 24 h and normalized.

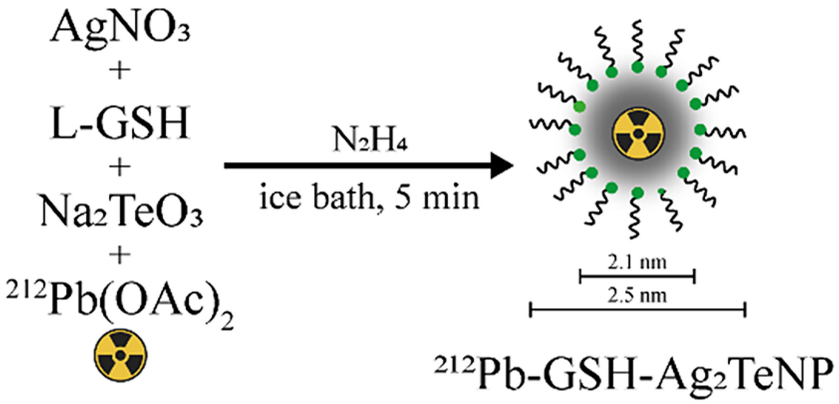

FIGURE 3 | Schematic illustration of the radiolabeling of GSH-Ag_2TeNPs with ^{212}Pb. ^{212}Pb was radiolabeled via a chelator-free method during the synthesis of GSH-Ag_2TeNPs.

TABLE 1 | An overview of the radiolabeling efficiency and radiochemical stability of ^{212}Pb- and ^{111}In-radiolabeled GSH-Ag_2TeNPs.

Radionuclide	Radiolabeling efficiency (%)	4 h RCS (%)	24 h RCS (%)
^{212}Pb[a]	75 ± 4	103 ± 5	96 ± 6
^{111}In	73 ± 2	—	91 ± 1

[a]The radiochemical stability (RCS) was determined as the sum of ^{212}Pb and ^{212}Bi by iTLC.

To verify this assumption, we first performed a pilot experiment with nonradioactive Pb $(NO_3)_2$ to check the feasibility of incorporating Pb in the GSH-Ag_2TeNPs. As shown in Figure S2, the ^{nat}Pb-GSH-Ag_2TeNPs had the same diameter as GSH-Ag_2TeNPs (2.1 ± 0.3 nm) and a hydrodynamic size of 2.7 ± 0.6 nm when using an initial Pb to Ag feeding ratio of 1–1000 (n/n). To predict the radiolabeling efficiency of ^{212}Pb, the conversion rate of $^{nat}Pb^{2+}$ and Ag^+ ions during the formation of the nanoparticles was determined by ICP-MS. A comparable conversion rate of about 70% was achieved for both Pb and Ag (Figure S3), probably due to the quenching of reaction at relatively early time point (5 min after the addition of hydrazine). Higher conversion rate is likely achievable by extending the reaction time, but that also leads to increase in the size of the nanoparticles [30]. To maintain the renal clearance properties of the GSH-Ag_2TeNPs, we decided to proceed with the ^{212}Pb-radiolabeling using a reaction time of 5 min, although the radiolabeling efficiency might be suboptimal. It has to be mentioned that according to the results of this pilot study, the maximum specific activity of the [^{212}Pb]Pb-GSH-Ag_2TeNPs is roughly estimated to be as high as 64 GBq/mg of Ag_2Te or 1.5 GBq/nmol of [^{212}Pb]Pb-GSH-Ag_2TeNPs. Detailed calculations can be found in the Supporting Information.

According to this established method, the [^{212}Pb]Pb-GSH-Ag_2TeNPs were prepared by exchanging ^{nat}Pb $(NO_3)_2$ by ^{212}Pb$(OAc)_2$. The radiolabeling efficiency was determined to be 75%, consistent with the results from the pilot study (Table 1). The change of the nitrate anions to acetate showed no effect on the incorporation of Pb into the Ag_2TeNPs.

3.4 | RCS of [^{212}Pb]Pb-GSH-Ag_2TeNPs

When ^{212}Pb decays to ^{212}Bi, the excitation energy can be released by the emission of γ photons but also via the ejection of an inner shell (K or L) electron, which leads to the creation of an electron vacancy. The electrons from outer shells will then transit

to fill in this vacancy, resulting in the emission of characteristic X-rays or Auger electrons or both, which leads to the creation of more electron vacancies. A cascade of Auger electrons eventually leads to the loss of a high number of electrons from the ^{212}Bi atoms, making the $^{212}Bi^{n+}$ ions highly positively charged ($n > 3$). A possible mechanism for the release of ^{212}Bi from the carrier molecules (e.g., DOTA) is the repulsive force between the $^{212}Bi^{3+}$ ions and the positively charged carriers after the donation of electrons to the $^{212}Bi^{n+}$ ions [27].

In this work, we developed the chelator-free labeling of ^{212}Pb on ultrasmall GSH-Ag_2TeNPs. As the dissociated $^{212}Pb^{2+}$ and $^{212}Bi^{3+}$ ions are not likely to be reabsorbed by the nanoparticles, all free $^{212}Pb^{2+}$ and ^{212}Bi should be easily separated from the nanoparticles using iTLC. The RCS can be calculated by comparing the retained ^{212}Pb/^{212}Bi in the nanoparticles with the free ^{212}Pb/^{212}Bi captured by excess of the ligand EDTA. After being challenged with 1 mM EDTA for 4 h or 24 h, RCS of the [^{212}Pb]Pb-GSH-Ag_2TeNPs was found to be nearly 100% and 96%, respectively (Table 1). The high RCS achieved from the [^{212}Pb]Pb-GSH-Ag_2TeNPs indicated the strong retention of ^{212}Pb and the internally converted ^{212}Bi. The high RCS of ^{212}Pb is likely to originate from the fact that PbTe is highly insoluble in water [40]. In terms of ^{212}Bi, the free electrons from the surrounding Ag atoms might rapidly migrate to the $^{212}Bi^{n+}$ ($n > 3$) ions, compensating the loss of electrons thus avoiding the ejection of ^{212}Bi from the nanoparticles [29, 38, 39].

3.5 | Preparation of [^{111}In]In-DTPA-Ag_2TeNPs

Despite the promising radiolabeling efficiency and high RCS, the specific activity of the [^{212}Pb]Pb-GSH-Ag_2TeNPs was not satisfying due to the low ^{212}Pb activity per sample (in kBq/μM nanoparticles) and the rather limited supply of ^{212}Pb. Thus, to determine the in vitro cellular uptake of the [^{212}Pb]Pb-GSH-Ag_2TeNPs, it was decided to perform the biological studies using ^{111}In as a radiotracer. For this purpose, DTPA was conjugated on the surface of the GSH-Ag_2TeNPs to allow radiolabeling with ^{111}In. The conjugation of DTPA was found to have minor effect on the size of the Ag_2TeNPs as determined by DLS and UV-vis measurements (Figure S4). The radiolabeling efficiency of ^{111}In on the DTPA-Ag_2TeNPs was found to be 73% with a 24 h RCS of 91% in PBS.

3.6 | Biocompatibility Study

Before performing the biological studies, the biocompatibility of GSH-Ag_2TeNPs, ^{nat}Pb-GSH-Ag_2TeNPs, and DTPA-modified GSH-Ag_2TeNPs was evaluated. The viability of U87 cells was measured after being incubated with either type of nanoparticles for 24 h. As shown in Figure S5, all nanoparticles were found to be nontoxic to cells at all tested concentrations.

3.7 | In Vitro Uptake and Subcellular Distribution of [^{111}In]In-DTPA-Ag_2TeNPs

The uptake and subcellular distribution of [^{111}In]In-DTPA-Ag_2TeNPs in 2D U87 cells were determined after incubating the cells with 10, 50, or 100 nM of nanoparticles for 4 or 24 h (Figure 4). The uptake of [^{111}In]In-DTPA-Ag_2TeNPs was found to be around 0.1% of the initially added ^{111}In activity after 4 h of incubation. The uptake increased to about 0.15% after extending the incubation time to 24 h and remained comparable to that of [^{111}In]In-DTPA (Figure 4a). The number of internalized [^{111}In]In-DTPA-Ag_2TeNPs per cell was also calculated based on the percentage of internalized ^{111}In activity, and it was found to be in the order of 10^5 nanoparticles/cell depending on the initial nanoparticle concentration (Figure 4b).

The subcellular distribution of the [^{111}In]In-DTPA-Ag_2TeNPs was further studied by cell fractionation experiments. As shown in Figure 4c, approximately 25% of the internalized [^{111}In]In-DTPA-Ag_2TeNPs were found to accumulate in the cell nucleus (24 h of incubation). The degree of [^{111}In]In-DTPA-Ag_2TeNPs uptake in the nucleus was surprisingly high and even comparable to some of the nucleus-targeting peptides radiolabeled with ^{111}In [41–43].

The results from in vitro uptake experiments suggest that these small GSH-Ag_2TeNPs are likely to be very efficient in cell killing if radiolabeled with ^{212}Pb due to their accumulation in the cell nucleus. To determine any possible difference between the uptake of ^{111}In- and ^{212}Pb-radiolabeled nanoparticles, further uptake studies should be performed with Pb isotopes such as ^{203}Pb using both in vitro and in vivo models. Higher retention and thereby possibly higher cell uptake can be expected by the

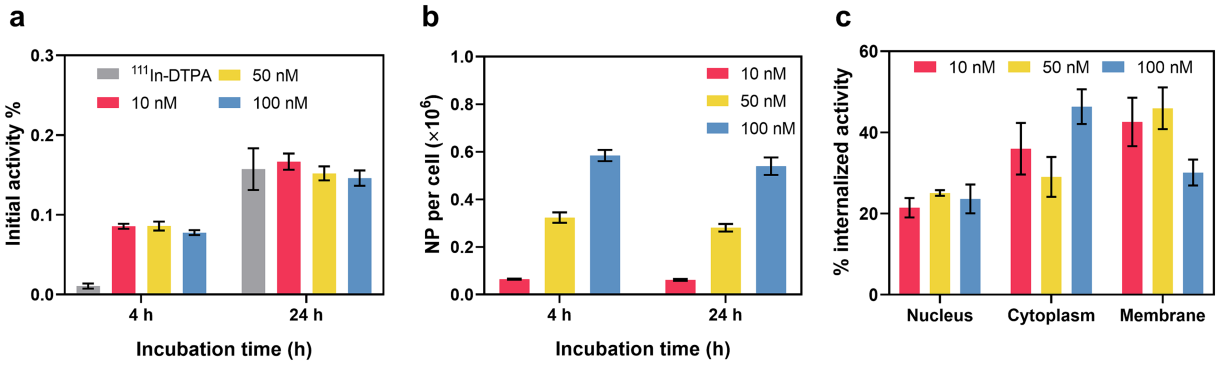

FIGURE 4 | In vitro uptake of the [^{111}In]In-DTPA-Ag_2TeNPs in 2D U87 cells using various nanoparticle concentrations and incubation time of 4 or 24 h. (a) Total uptake of [^{111}In]In-DTPA-Ag_2TeNPs in U87 cell monolayers. The uptake of [^{111}In]In-DTPA using the same ^{111}In activity was also measured for comparison. The results are presented as percentage of the initially added activity, $n = 3$; (b) internalized [^{111}In]In-DTPA-Ag_2TeNPs per cell, $n = 3$; (c) percentage of [^{111}In]In-DTPA-Ag_2TeNPs located in the cell nucleus, cytoplasm, and membrane determined by subcellular fractionation, $n = 3$.

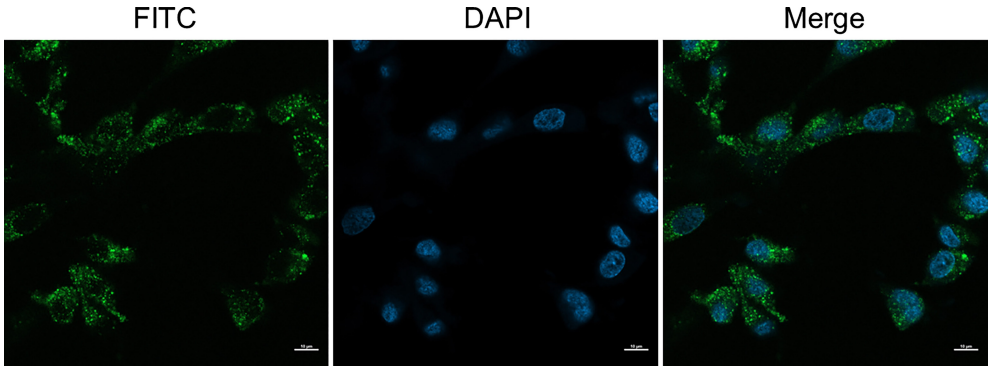

FIGURE 5 | Confocal images of U87 cells after 24 h of incubation with FITC-Ag_2TeNPs. The concentration of the NPs was 100 nM. The cell nucleus was stained by DAPI (blue, middle) while the FITC-Ag_2TeNPs showed a green fluorescence (left). The merged image (right) indicates the colocalization of FITC-Ag_2TeNPs and the cell nucleus. Scale bar = 10 μm. [Correction added on 21 August 2024, after first online publication: the Figure 5 has been corrected in this version].

conjugation of tumor targeting moieties on the nanoparticle surface while maintaining their small hydrodynamic diameters.

3.8 | Confocal Microscopy

To further confirm the localization of the nanoparticles in U87 cells, we modified the GSH-Ag_2TeNPs with FITC and checked their distribution in U87 cells using confocal microscopy. The linkage of FITC was achieved by the NHS-amine reaction taking advantage of the high number of free amine groups available from the GSH coating. The successful FITC modification was verified by measuring the emission spectrum and the UV-vis spectrum of FITC-Ag_2TeNPs (Figure S6). The confocal images shown in Figure 5 revealed that the FITC signal can be observed in the cell nucleus. In addition to the nucleus, even stronger FITC signal was observed in the cytoplasm and the cell membrane, matching well with the results of the subcellular fractionation assays.

3.9 | In Vitro Tumor Killing Efficiency of [^{111}In]In-DTPA-Ag_2TeNPs

Considering the nucleus uptake, we decided to evaluate the tumor killing efficiency of the [^{111}In]In-DTPA-Ag_2TeNPs by performing a colony formation assay to further prove the nucleus accumulation of these small nanoparticles. During the decay of ^{111}In, there are on average 7.4 Auger electrons coemitted along with the photons [44]. Thus, high tumor killing efficiency can be expected if the [^{111}In]In-DTPA-Ag_2TeNPs accumulate in the cell nucleus after internalization. As shown in Figure 6, the surviving fraction of U87 cells treated with 2 or 3 MBq of [^{111}In]In-DTPA-Ag_2TeNPs significantly decreased compared to that of untreated cells ($p < 0.001$ for the 2 MBq group, $p < 0.0001$ for the 3 MBq group, one-way ANOVA test). Meanwhile, the treatment with the 3 MBq of [^{111}In]In-DTPA only decreased the cell surviving fraction by 15%, indicating the vital role of the small nanoparticles in cell killing. Based on the results of this cytotoxicity assay, the nucleus localization of the [^{111}In]In-DTPA-Ag_2TeNPs was indirectly confirmed.

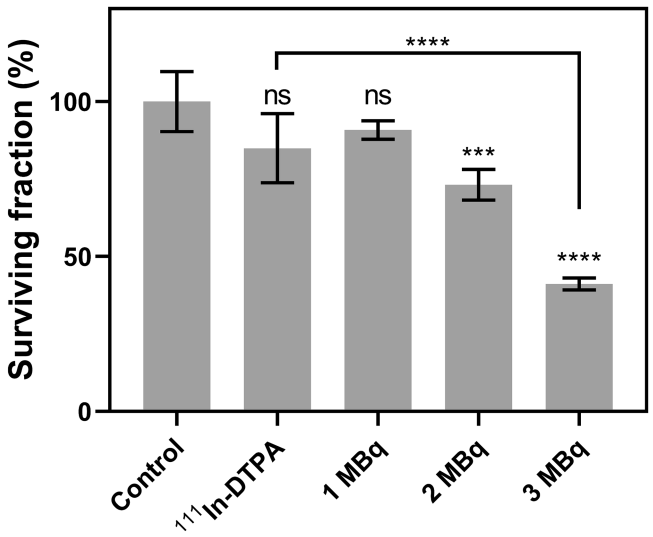

FIGURE 6 | In vitro tumor cell killing efficiency of [^{111}In]In-DTPA-Ag_2TeNPs as determined by colony formation assay after 24 h of incubation with [^{111}In]In-DTPA-Ag_2TeNPs containing ^{111}In activity ranging from 1 to 3 MBq. The tumor killing efficiency of [^{111}In]In-DTPA (3 MBq) was also measured for comparison, $n = 3$. The specific activity of [^{111}In]In-DTPA-Ag_2TeNPs was 11.9 kBq/nM. p values: ns $p > 0.05$, ***$p \leq 0.001$, and ****$p \leq 0.0001$.

4 | Conclusion

In summary, we developed a novel ^{212}Pb/^{212}Bi in vivo generator by combining ^{212}Pb and small GSH-Ag_2TeNPs, enabling high RCS and tumor cell nucleus accumulation. The experiments using ^{111}In showed that these particles are able to induce cell death, which implies that when applying ^{212}Pb, even higher killing efficiencies can be reached. Unfortunately, the limited availability of ^{212}Pb did not allow us to validate this hypothesis. Considering the extra benefits of these nanoparticles such as the potential renal clearance and the possibility of being coradiolabeled by ^{203}Pb for SPECT imaging, the [^{212}Pb]Pb-GSH-Ag_2TeNPs might provide a new opportunity to develop a theragnostic agent for RNT. For eventual clinical applications,

the [^{212}Pb]Pb-GSH-Ag_2TeNPs can be functionalized by tumor targeting moieties which are currently under development in our group.

Author Contributions

A.G.D. and H.T.W. contributed to the design and supervision of this work. R.W. designed and carried out the experiments, analyzed the results, and prepared the first draft of the manuscript. All authors read and approved the final manuscript.

Acknowledgements

The authors would like to thank Dr. Erik de Blois from Erasmus Medical Center for providing ^{111}In.

Ethics Statement

The authors have nothing to report.

Conflicts of Interest

The authors declare no conflicts of interest.

Data Availability Statement

The data that support the findings of this study are available in the supplementary material of this article.

References

1. A. Dash, F. F. Knapp, and M. Pillai, "Targeted Radionuclide Therapy-An Overview," *Current Radiopharmaceuticals* 6, no. 3 (2013): 152–180.

2. G. Sgouros, L. Bodei, M. R. McDevitt, and J. R. Nedrow, "Radiopharmaceutical Therapy in Cancer: Clinical Advances and Challenges," *Nature Reviews. Drug Discovery* 19, no. 9 (2020): 589–608.

3. J. P. Pouget and S. J. Mather, "General Aspects of the Cellular Response to Low- and High-LET Radiation," *European Journal of Nuclear Medicine* 28, no. 4 (2001): 541–561.

4. M. R. Zalutsky and O. R. Pozzi, "Radioimmunotherapy With Alpha-Particle Emitting Radionuclides," *The Quarterly Journal of Nuclear Medicine and Molecular Imaging* 48, no. 4 (2004): 289–296.

5. G. Sgouros, J. C. Roeske, M. R. McDevitt, et al., "MIRD Pamphlet No. 22 (Abridged): Radiobiology and Dosimetry of α-Particle Emitters for Targeted Radionuclide Therapy," *Journal of Nuclear Medicine* 51, no. 2 (2010): 311–328.

6. K. A. Morgan, S. E. Rudd, A. Noor, and P. S. Donnelly, "Theranostic Nuclear Medicine With Gallium-68, Lutetium-177, Copper-64/67, Actinium-225, and Lead-212/203 Radionuclides," *Chemical Reviews* 123, no. 20 (2023): 12004–12035.

7. D. E. Milenic, K. Garmestani, E. D. Brady, et al., "α-Particle Radioimmunotherapy of Disseminated Peritoneal Disease Using a ^{212}Pb-Labeled Radioimmunoconjugate Targeting HER2," *Cancer Biotherapy & Radiopharmaceuticals* 20, no. 5 (2005): 557–568.

8. V. Boudousq, L. Bobyk, M. Busson, et al., "Comparison Between Internalizing Anti-HER2 mAbs and Non-Internalizing Anti-CEA mAbs in Alpha-Radioimmunotherapy of Small Volume Peritoneal Carcinomatosis Using ^{212}Pb," *PLoS ONE* 8, no. 7 (2013): e69613.

9. K. J. Yong, D. E. Milenic, K. E. Baidoo, Y. S. Kim, and M. W. Brechbiel, "Gene Expression Profiling Upon ^{212}Pb-TCMC-Trastuzumab Treatment in the LS-174T i.p. Xenograft Model," *Cancer Medicine* 2, no. 5 (2013): 646–653.

10. D. E. Milenic, K. E. Baidoo, Y.-S. Kim, and M. W. Brechbiel, "Evaluation of Cetuximab as a Candidate for Targeted α-Particle Radiation Therapy of HER1-Positive Disseminated Intraperitoneal Disease," *MAbs* 7, no. 1 (2015): 255–264.

11. B. B. Kasten, M. T. Azure, T. R. Schoeb, D. R. Fisher, and K. R. Zinn, "Imaging, Biodistribution, and Toxicology Evaluation of ^{212}Pb-TCMC-Trastuzumab in Nonhuman Primates," *Nuclear Medicine and Biology* 43, no. 7 (2016): 391–396.

12. B. B. Kasten, P. G. Oliver, H. Kim, et al., "^{212}Pb-Labeled Antibody 225.28 Targeted to Chondroitin Sulfate Proteoglycan 4 for Triple-Negative Breast Cancer Therapy in Mouse Models," *International Journal of Molecular Sciences* 19, no. 4 (2018): 925.

13. I. Liatsou, J. Yu, R. Bastiaannet, et al., "^{212}Pb-Conjugated Anti-Rat HER2/neu Antibody Against a neu-N Derived Murine Mammary Carcinoma Cell Line: Cell Kill and RBE in Vitro," *International Journal of Radiation Biology* 98, no. 9 (2022): 1452–1461.

14. Y. Miao, M. Hylarides, D. R. Fisher, et al., "Melanoma Therapy via Peptide-Targeted α-Radiation," *Clinical Cancer Research* 11, no. 15 (2005): 5616–5621.

15. M. Li, D. Liu, D. Lee, et al., "Targeted Alpha-Particle Radiotherapy and Immune Checkpoint Inhibitors Induces Cooperative Inhibition on Tumor Growth of Malignant Melanoma," *Cancers (Basel)* 13, no. 15 (2021): 3676.

16. B. B. Kasten, A. Gangrade, H. Kim, et al., "^{212}Pb-Labeled B7-H3-Targeting Antibody for Pancreatic Cancer Therapy in Mouse Models," *Nuclear Medicine and Biology* 58 (2018): 67–73.

17. D. Bauer, L. M. Carter, M. I. Atmane, et al., "^{212}Pb-Pretargeted Theranostics for Pancreatic Cancer," *Journal of Nuclear Medicine* 65, no. 1 (2023): 109–116.

18. T. A. R. Stallons, A. Saidi, I. Tworowska, E. S. Delpassand, and J. J. Torgue, "Preclinical Investigation of ^{212}Pb-DOTAMTATE for Peptide Receptor Radionuclide Therapy in a Neuroendocrine Tumor Model," *Molecular Cancer Therapeutics* 18, no. 5 (2019): 1012–1021.

19. D. Chapeau, S. Koustoulidou, M. Handula, et al., "[^{212}Pb]Pb-eSOMA-01: A Promising Radioligand for Targeted Alpha Therapy of Neuroendocrine Tumors," *Pharmaceuticals (Basel)* 16, no. 7 (2023): 985.

20. S. D. Ebrahim, T. Izabela, E. Rouzbeh, et al., "Targeted α-Emitter Therapy With ^{212}Pb-DOTAMTATE for the Treatment of Metastatic SSTR-Expressing Neuroendocrine Tumors: First-in-Humans Dose-Escalation Clinical Trial," *Journal of Nuclear Medicine* 63, no. 9 (2022): 1326–1333.

21. B. B. Kasten, R. C. Arend, A. A. Katre, et al., "B7-H3-Targeted ^{212}Pb Radioimmunotherapy of Ovarian Cancer in Preclinical Models," *Nuclear Medicine and Biology* 47 (2017): 23–30.

22. R. Meredith, J. Torgue, S. Shen, et al., "Dose Escalation and Dosimetry of First-in-Human Alpha Radioimmunotherapy With ^{212}Pb-TCMC-Trastuzumab," *Journal of Nuclear Medicine* 55, no. 10 (2014): 1636–1642.

23. R. F. Meredith, J. Torgue, M. T. Azure, et al., "Pharmacokinetics and Imaging of ^{212}Pb-TCMC-Trastuzumab After Intraperitoneal Administration in Ovarian Cancer Patients," *Cancer Biotherapy & Radiopharmaceuticals* 29, no. 1 (2014): 12–17.

24. A. Corroyer-Dulmont, S. Valable, N. Falzone, et al., "VCAM-1 Targeted Alpha-Particle Therapy for Early Brain Metastases," *Neuro-Oncology* 22, no. 3 (2020): 357–368.

25. Y. Miao, S. D. Figueroa, D. R. Fisher, et al., "^{203}Pb-Labeled Alpha-Melanocyte-Stimulating Hormone Peptide as an Imaging Probe for Melanoma Detection," *Journal of Nuclear Medicine* 49, no. 5 (2008): 823–829.

26. M. Li, N. J. Baumhover, D. Liu, et al., "Preclinical Evaluation of a Lead Specific Chelator (PSC) Conjugated to Radiopeptides for ^{203}Pb and ^{212}Pb-Based Theranostics," *Pharmaceutics.* 15, no. 2 (2023): 414.

27. S. Mirzadeh, K. Kumar, and O. A. Gansow, "The Chemical Fate of ^{212}Bi-DOTA Formed by β- Decay of ^{212}Pb(DOTA)^{2}," *Radiochimica Acta* 60, no. 1 (1993): 1–10.

28. D. Beninson, H. Dunster, W. Jacobi, et al., "Limits for Intakes of Radionuclides by Workers," *Annals of the ICRP* 67 (1980): 67–68.

29. R. Wang, B. Ponsard, H. Wolterbeek, and A. Denkova, "Core–Shell Structured Gold Nanoparticles as Carrier for ^{166}Dy/^{166}Ho In Vivo Generator," *EJNMMI Radiopharmacy and Chemistry* 7, no. 1 (2022): 16.

30. L. M. Nieves, Y. C. Dong, D. N. Rosario-Berrios, et al., "Renally Excretable Silver Telluride Nanoparticles as Contrast Agents for X-Ray Imaging," *ACS Applied Materials & Interfaces* 14, no. 30 (2022): 34354–34364.

31. M. J. Mitchell, M. M. Billingsley, R. M. Haley, M. E. Wechsler, N. A. Peppas, and R. Langer, "Engineering Precision Nanoparticles for Drug Delivery," *Nature Reviews. Drug Discovery* 20, no. 2 (2021): 101–124.

32. K. M. Tsoi, S. A. MacParland, X. Z. Ma, et al., "Mechanism of Hard-Nanomaterial Clearance by the Liver," *Nature Materials* 15, no. 11 (2016): 1212–1221.

33. B. Du, M. Yu, and J. Zheng, "Transport and Interactions of Nanoparticles in the Kidneys," *Nature Reviews Materials* 3, no. 10 (2018): 358–374.

34. K. Huang, H. Ma, J. Liu, et al., "Size-Dependent Localization and Penetration of Ultrasmall Gold Nanoparticles in Cancer Cells, Multicellular Spheroids, and Tumors in Vivo," *ACS Nano* 6, no. 5 (2012): 4483–4493.

35. S. Huo, S. Jin, X. Ma, et al., "Ultrasmall Gold Nanoparticles as Carriers for Nucleus-Based Gene Therapy due to Size-Dependent Nuclear Entry," *ACS Nano* 8, no. 6 (2014): 5852–5862.

36. V. R. Patel and Y. K. Agrawal, "Nanosuspension: An Approach to Enhance Solubility of Drugs," *Journal of Advanced Pharmaceutical Technology & Research* 2, no. 2 (2011): 81–87.

37. K. P. García, K. Zarschler, L. Barbaro, et al., "Zwitterionic-Coated "Stealth" Nanoparticles for Biomedical Applications: Recent Advances in Countering Biomolecular Corona Formation and Uptake by the Mononuclear Phagocyte System," *Small* 10, no. 13 (2014): 2516–2529.

38. A. W. Adamson and J. M. Grunland, "Retention of ^{80}Br in Complex Bromides, Following Isomeric Transition," *Journal of the American Chemical Society* 73, no. 11 (1951): 5508.

39. S. Wexler and G. Anderson, "Dissociation of Methyl Bromide by Nuclear Isomeric Transition of 4.4-hr ^{80m}Br," *Journal of Chemical Physics* 33, no. 3 (1960): 850–863.

40. J. He, M. G. Kanatzidis, and V. P. Dravid, "High Performance Bulk Thermoelectrics via a Panoscopic Approach," *Materials Today* 16, no. 5 (2013): 166–176.

41. V. J. Facca, Z. Cai, N. E. K. Gopal, and R. M. Reilly, "Panitumumab-DOTA-^{111}In: An Epidermal Growth Factor Receptor Targeted Theranostic for SPECT/CT Imaging and Meitner-Auger Electron Radioimmunotherapy of Triple-Negative Breast Cancer," *Molecular Pharmaceutics* 19, no. 10 (2022): 3652–3663.

42. B. Cornelissen, A. Waller, C. Target, V. Kersemans, S. Smart, and K. A. Vallis, "^{111}In-BnDTPA-F3: An Auger Electron-Emitting Radiotherapeutic Agent That Targets Nucleolin," *EJNMMI Research* 2, no. 1 (2012): 9.

43. B. Cornelissen, M. Hu, K. McLarty, D. Costantini, and R. M. Reilly, "Cellular Penetration and Nuclear Importation Properties of ^{111}In-Labeled and ^{123}I-Labeled HIV-1 Tat Peptide Immunoconjugates in BT-474 Human Breast Cancer Cells," *Nuclear Medicine and Biology* 34, no. 1 (2007): 37–46.

44. K. F. Eckerman and A. Endo, *MIRD Radionuclide Data and Decay Schemes* (Reston (VA): The Society of Nuclear Medicine, 2007).

Supporting Information

Additional supporting information can be found online in the Supporting Information section.